



Hydrothermal performance of a turbulent nanofluid with different nanoparticle shapes in a duct fitted with various configurations of coiled-wire inserts

Amro H. Al-Tohamy¹ · Olatomide G. Fadodun² · Amr Kaood³

Received: 23 December 2022 / Accepted: 23 April 2023 / Published online: 29 May 2023
© The Author(s) 2023

Abstract

This paper examines the turbulent hydrothermal performance of boehmite/water–ethylene glycol (γ – AlO(OH)/H₂O – EG) nanofluid flowing through a square duct fitted with various coiled-wire inserts (CWIs) using the finite volume method. The turbulent flow of γ – AlO(OH)/H₂O – EG nanofluid is modeled using single-phase and $k - \epsilon$ model. A parametric study is carried out on the effect of Reynolds number ($5.0 \times 10^3 \leq Re \leq 4.0 \times 10^4$), the geometry of wire (circular, triangular, square, square-diamond, hexagon, octagon, and decagon), nanoparticle volume ratio ($0 \leq \varphi \leq 4\%$), and nanoparticle shapes (blade, brick, cylinder, platelet, and oblate-spheroid) on hydrodynamic and convective heat transfer performance (CHTP). The results showed that the combination between CWI and nanofluid enhances hydrothermal performance. For instance, among the geometries of CWI considered at $Re = 5.0 \times 10^3$, the square CWI has the highest normalized Nu^G (referencing empty channel) of 2.58, while the decagon has the lowest value of 1.78. Furthermore, regarding the nanoparticle shapes, the platelet shape has a maximum normalized Nu^N (referencing base fluid) of 1.53, while the oblate-spheroid has a minimum value of 0.93. Lastly, in terms of application, square and octagon wire-fitted channels are better than empty channel at low Re , as the values of their hydrothermal performance evaluation criteria are greater than unity.

Keywords Nusselt number · Friction factor · Nanoparticle shapes · Square channel heat exchanger · Coiled-wire insert · Performance evaluation criteria

Introduction

Enhancement of convective heat transfer performance (CHTP) is indispensable toward achieving optimization and miniaturization of the thermal system. Generally, CHTP in a thermal system can be enhanced using active, passive, and compound methods. The active methods require external power for its operation, while the passive method, which is principally a modification of geometry or fluid properties (like the usage of nanofluid), does not require external

power for its operation [1–4]. Last decades, many authors investigated various techniques of heat transfer enhancement such as corrugated tubes [5–7], twisted-tape inserts [8, 9], dimpled tubes [10], conical tubes [11], coil inserts [12, 13], nanofluids [14, 15], conical inserts [16], fins [17], and fluid injection [18, 19]. The physics behind the enhancement of CHTP due to geometry modification lies in the fact that the thinner the thickness of the thermal boundary layer (δ_{th}), the better the rate of CHTP. Therefore, the geometry of the thermal system is modified such that the δ_{th} of the fluid reduces along the flow direction [20–23].

The literature survey showed that a channel fitted with CWI is preferable among various geometry modifications examined so far because of its improved heat transfer performance and ease of fabrication and maintenance. Furthermore, it has a variety of industrial applications. Admane and Patil [24] experimentally investigated turbulent CHTP of distilled water flowing through a heat exchanger fitted with CWI. The study examined the effect of different pitch ratios for the insert on the Nusselt number (Nu) and friction factor

✉ Amr Kaood
aki03@fayoum.edu.eg

¹ Mechanical Engineering Department, Higher Technological Institute, 6th of October Branch, Giza 12596, Egypt

² Centre for Energy Research and Development, Obafemi Awolowo University, Ife, Nigeria

³ Mechanical Engineering Department, Faculty of Engineering, Fayoum University, El-Fayoum 63514, Egypt

(fr) at Re between 4000 and 14,000. They concluded that the presence of CWI and decrease in its pitch enhances thermal performance. Shoji et al. [25] performed experiments to examine the laminar CHTP of water flowing through a pipe with a copper-made CWI. The work examined the influence of the length of the CWI on dP and Nu. The authors reported that at low Re, the length of the CWI is not sensitive to Nu. However, at high Re, the Nu increases as the wire's length increases. Naphon [26] carried out an experimental study on the hydrothermal performance of water flowing in a concentric pipe fitted with a bended CWI. The study focused on the effect of Re and pitch of the inserted turbulator on Nu and dP. The researcher posited that the insert had significant role on the enhancement of CHTP. Furthermore, an increase in the pitch of the iron-made CWI reduces both Nu and dP. Finally, a correlation for Nu as a function of pitch and Re was introduced. Keklikcioglu and Ozceyhan [12] conducted experiments to investigate the effect of Re, pitch-to-diameter ratio (P/D) of equilateral triangular cross-section CWI, and clearance (distance between the WCI and the inner wall of the pipe) on the average Nu and fr of water flowing inside circular pipe. The authors reported an optimum configuration with thermal performance evaluation criterion (PEC) of 1.8. Furthermore, they reported that decrease in P/D of the CWI and clearance distance enhances both Nu and fr. Abbaspour et al. [27] compared turbulent CHTP of water flowing inside a straight tube fitted with conical rings and CWI with the empty straight tube. The numerical study considered the effect of coil diameter and pitch on Nu and fr. The authors concluded that increase in diameter of the coil by 300% enhances Nu by 131%, while 37.5% decrease in value of the pitch increases the Nu by 143%. Abedin and Shakar [28] performed an experimental analysis to investigate the effect of the pitch of the CWI with corresponding helix angles on Nu and dP for a fully developed turbulent airflow through a pipe. The author reported that a low Re, a maximum ratio of 2 and 4, was reached against Nu and dP, respectively, while the maximum thermal enhancement factor was 1.25. Wahidifar and Kohrom [29] conducted experiments to study the thermal behavior and the pressure drop of water flowing through a horizontal heat exchanger fitted with a coiled-wire and rings inserts. The study focused on the effect of the pitch-to-coil diameter ratio and the wire-to-coil diameter ratio on the PEC. They presented the optimum configuration, which has a PEC value of 1.28 at Re = 10,000. Ali et al. [30] also studied experimentally the effect of the geometric parameters (ratio of pitch-to-coil diameter and ratio of wire diameter-to-coil diameter) on CHTP of air flowing through a copper tube fitted with helical-coil insert across a range of Re ($14200 \leq Re \leq 49800$). The authors reported 82% increment in Nu.

As stated earlier, another means of enhancing CHTP is by replacing the conventional heat transfer fluid with a

nanofluid. Nanofluid is a type of improved heat transfer fluid obtained by dispersing small amounts of nanoparticles of higher thermal conductivity (SiO_2 , Al_2O_3 , TiO_2 , and Fe_2O_3) in base fluid (water and ethylene glycol). These resultant fluids have better thermophysical properties (thermal conductivity) than the base fluid [31–33]. Furthermore, it has been shown by various researchers that the nanoparticle's shape has an influence on its CHTP [34, 35]. For instance, Benkhedda et al. [36] numerically examined the influence of nanoparticle shapes (platelet, cylindrical, blade, and spherical) of $\text{TiO}_2/\text{H}_2\text{O}$ nanofluid on hydrodynamic and CHTP. They revealed that among the four nanoparticle shapes considered, the blade nanoparticle has the highest Nu while spherical shape has the lowest. Experiments by Jeong et al. [37] were performed to examine the influence of nanoparticle shapes (nearly rectangular and spherical) on the viscosity and thermal conductivity of $\text{ZnO}/\text{H}_2\text{O}$. The results mentioned that the nearly rectangular nanoparticle has a higher viscosity and thermal conductivity than nanoparticles of spherical shape. In another study, an experimental analysis of the effect of the nanoparticle shape of $\text{ZnO}/\text{H}_2\text{O}$ and $\text{SiO}_2/\text{H}_2\text{O}$ on CHTP and energetic performance was conducted by Ferrouillat et al. [38]. The authors concluded that the shape of a nanoparticle affects both Nu and fr. A detailed experimental work by Maheshwary et al. [39] investigated the impact of nanoparticle's concentration, shape (cubic, rod, and spherical), and size on thermophysical properties of $\text{TiO}_2/\text{H}_2\text{O}$ nanofluid and its CHTP. The researchers disclosed that nanoparticle shapes enhanced the thermal conductivity by 5.62% over the base fluid. Furthermore, the cubic nanoparticle has the highest pumping power among the aforementioned shapes, while the spherical nanoparticle has the lowest.

Based on this review, the following conclusion can be drawn:

1. There are a lot of existing works on CHTP due to CWI. However, the majority of these works only examined the traditional CWI of a circular shape [40].
2. The effect of nanoparticle shapes on the flow characteristics and the thermo-hydraulic performance has been studied by many researchers. However, there is no work in this literature review that has examined the nanoparticle shapes' impact (blade, brick, cylinder, oblate-spheroid, and platelet) on the hydrodynamic and CHTP of a nanofluid flow in a square channel fitted with CWI having various geometries (circular, triangular, square, square-diamond, hexagon, octagon, and decagon).

As a result of these aforementioned research gaps, this study aims to investigate the turbulent thermo-hydraulic performance of $\gamma - \text{AlO}(\text{OH})/\text{H}_2\text{O} - \text{EG}$ nanofluid, flowing through a square duct fitted with CWI having various

geometries by considering the effect of Re , nanoparticle shapes (blade, brick, cylinder, oblate-spheroid, and platelet), and shapes of the wire-coil (circular, triangular, square, square-diamond, hexagon, octagon, and decagon). The boehmite/water–ethylene glycol nanofluid has been chosen because its nanoparticles exist in various phases (shapes).

Materials and methods

Problem description

This study investigates the turbulent thermal–hydraulic performance of $\gamma - \text{AlO}(\text{OH})/\text{H}_2\text{O} - \text{EG}$ nanofluid flowing in a square duct with and without CWI and subjected to constant heat flux, as shown in Fig. 1. The square duct has a cross-section area of $0.1 \times 0.1 \text{ m}^2$ and 1-m long. The CWIs are of various geometries (circular, triangular, square, square-diamond, hexagon, octagon, and decagon), as shown in Fig. 2. The dimensions for the CWIs are mentioned in Table 1 and illustrated in Fig. 1b. Also, the boehmite/water–ethylene glycol nanofluid is prepared from nanoparticles of various shapes (blade, brick, cylinder, oblate-spheroid, and platelet), as shown in Fig. 3.

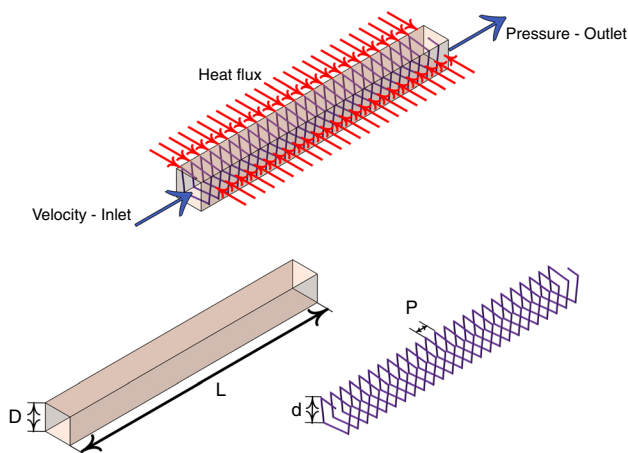


Fig. 1 a Schematic of the mathematical model with applied boundary conditions. b Geometrical parameters of duct and CWI

Table 1 Dimensions for the CWIs

Dimension	Value	Unit
Pitch (P)	0.004	m
Mean diameter (d)	0.10	m

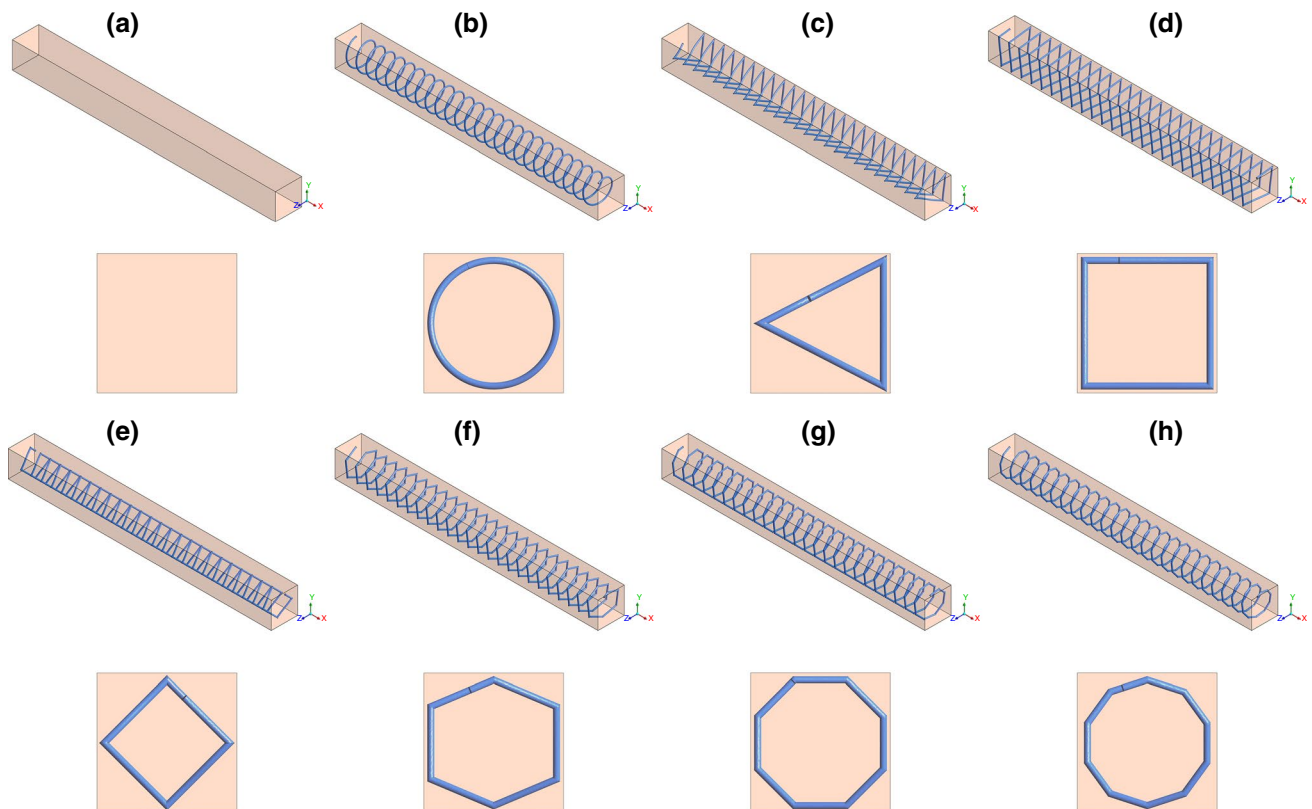


Fig. 2 Configuration of the square channel with CWI having various geometries. a Empty channel, b circular CW, c triangular CW, d square CW, e square-diamond CW, f hexagon CW, g octagon CW, and h decagon CW

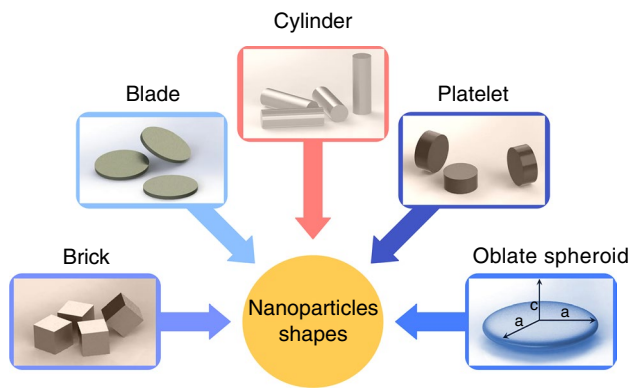


Fig. 3 Schematic for nanoparticle shapes used in the nanofluid [34]

In this study, the nanoparticles are assumed to be homogeneously mixed with the base fluid consisting of distilled water and ethylene glycol mixed together at an equal ratio (50:50). As a result, a single-phase model is used to model the nanofluid. The other assumptions regarding this model are available in the previous works [5, 11].

Governing equations

Considering the aforementioned system, a 3D model has been established to simulate turbulent flow through the different channel configurations under steady-state conditions. The control volume is governed by the following equations (continuity, momentum, energy, turbulence kinetic energy, dissipation rate, and turbulence kinetic energy (TKE)), which are expressed as follows [2, 11]:

Continuity equation:

$$\frac{\partial}{\partial x_i} (\rho_{nf} u_i) = 0 \quad (1)$$

Momentum equation:

$$\begin{aligned} \frac{\partial}{\partial x_i} (\rho_{nf} u_i u_j) = \frac{\partial}{\partial x_j} \left[\mu_{nf} \left(\frac{\partial u_i}{\partial x_j} + \frac{\partial u_j}{\partial x_i} - \frac{2}{3} \delta_{ij} \frac{\partial u_i}{\partial x_j} \right) \right] \\ + \frac{\partial}{\partial x_j} \left(-\rho' u_j u_i \right) - \frac{\partial P}{\partial x_i} \end{aligned} \quad (2)$$

Energy equation:

$$\frac{\partial}{\partial x_i} [u_i (\rho E + P)] = \frac{\partial}{\partial x_j} \left[\left(\lambda_{nf} + \frac{c_p \mu_t}{Pr_t} \right) \frac{\partial T}{\partial x_j} + u_i (\tau_{ij})_{eff} \right] = 0 \quad (3)$$

Here u_i and u_j are the nanofluid velocities in i and j direction, respectively. P , ρ , c_p , and T are the local nanofluid pressure, density, constant pressure specific heat, and temperature,

respectively. $E = c_p T - \frac{P}{\rho} + \frac{u^2}{2}$ represents the total energy, and $\rho u_j u_i$ is the Reynolds stress. Pr_t announces the turbulent Prandtl number, while the deviatoric tensor $(\tau_{ij})_{eff}$ is given as follows:

$$(\tau_{ij})_{eff} = \mu_{eff} \left[\left(\frac{\partial u_j}{\partial x_i} + \frac{\partial u_i}{\partial x_j} \right) - \frac{2}{3} \delta_{ij} \frac{\partial u_i}{\partial x_j} \right] \quad (4)$$

where μ_{eff} is the effective molecular viscosity and is denoted as follows:

$$\mu_{eff} = \mu_{nf} + \mu_t \quad (5)$$

In the previous equation, μ_{nf} and μ_t represent the dynamic and turbulent viscosities. The realizable $k - \epsilon$ turbulent model has been chosen based on other similar previous studies [41–43]. In addition, its superior prediction performance for the fluid flow involves recirculation, separation, rotation, and boundary layers under strong adverse pressure gradients [44]. The governing equation for the rate of production of turbulent kinetic energy (k) and the rate of dissipation (ϵ) are expressed in Eqs. (6 and 7), respectively [45].

$$\frac{\partial (\rho_{nf} k u_i)}{\partial x_i} = \frac{\partial}{\partial x_i} \left[\left(\mu_{nf} + \frac{\mu_t}{\sigma_k} \right) \frac{\partial k}{\partial x_i} \right] + G_k - \rho_{nf} \epsilon \quad (6)$$

$$\frac{\partial (\rho_{nf} \epsilon u_i)}{\partial x_i} = \frac{\partial}{\partial x_i} \left[\left(\mu_{nf} + \frac{\mu_t}{\sigma_{f\epsilon}} \right) \frac{\partial \epsilon}{\partial x_i} \right] + \rho_{nf} C_{1\epsilon} S \epsilon - C_{2\epsilon} \frac{\epsilon^2 \rho_{nf}}{k + \sqrt{\nu \epsilon}} \quad (7)$$

where G_k is the turbulence energy generation due to mean velocity gradients and is defined as follows:

$$G_k = \mu_t S^2 \quad (8)$$

With

$$\mu_t = \rho_{nf} C_\mu \frac{k^2}{\epsilon} \quad (9)$$

$$S = \sqrt{2 S_{ij} S_{ij}} \quad (10)$$

$$S_{ij} = 0.5 \left(\frac{\partial u_i}{\partial x_j} + \frac{\partial u_j}{\partial x_i} \right) \quad (11)$$

$$C_{1\epsilon} = \max \left[0.43, \frac{\eta}{\eta + 5} \right] \quad (12)$$

$$\eta = S \frac{k}{\epsilon} \quad (13)$$

Table 2 Realizable $k - \epsilon$ model constants [46]

Constant	$C_{2\epsilon}$	C_μ	σ_k	σ_ϵ
Value	1.9	0.09	1	1.2

Table 3 Summarize of boundary conditions

Region	Boundary conditions			
	Momentum	Thermal	Turbulence kinetic energy / k	Turbulent dissipation rate / ϵ
Inlet	Velocity-inlet	298 K	$\frac{3}{2}(Iu_{in})^2$	$\frac{c_\mu^{0.75}k^{1.5}}{0.07 \times D_h}$
Outlet	Pressure-outlet	-	$\frac{\partial k}{\partial x} = 0$	$\frac{\partial \epsilon}{\partial x} = 0$
Wall	No-slip condition	$q'' = 5.0 \times 10^4 \text{ W m}^{-2}$	-	-
CWI	No-slip condition	Adiabatic	-	-

The model constants ($C_{2\epsilon}$, C_μ , σ_k , and σ_ϵ) are provided in Table 2. Also, the flow conditions for the turbulent nanofluid are afforded in Table 3.

Nanofluid description

As stated earlier, the $\gamma - \text{AlO}(\text{OH})/\text{H}_2\text{O} - \text{EG}$ nanofluid has been prepared from boehmite ($\gamma - \text{AlO}(\text{OH})$) nanoparticles of various shapes (blade, brick, cylinder, oblate-spheroid, and platelet). The nanofluid's thermophysical properties (thermal conductivity and viscosity) largely depend on their shapes. Thus, the thermal conductivity (λ_{nf}) of nanofluid prepared from blade, brick, cylinder, and platelet nanoparticles is estimated using the following formula [47].

$$\frac{\lambda_{nf}}{\lambda_f} = 1 + \left(C_k^{shape} + C_k^{surface} \right) \varphi = 1 + C_k \varphi \tag{14}$$

While the corresponding viscosities (μ_{nf}) are estimated using

$$\frac{\mu_{nf}}{\mu_f} = \left(1 + A_1 \varphi + A_2 \varphi^2 \right) \tag{15}$$

where the φ , nf , and f represent the nanoparticle volume ratio (VR), the nanofluid, and the $\text{H}_2\text{O} - \text{EG}$ (50:50) base fluid, respectively. The aspect ratio of these nanoparticles and the values for their C_k^{shape} , $C_k^{surface}$, and C_k are listed in Table 4. The factors A_1 and A_2 are given in Table 5.

For oblate-spheroid nanoparticles, the thermal conductivity (λ_{nf}) and viscosity (μ_{nf}) are estimated as follows [49]:

Table 4 Aspect ratio and values for essential factors employed in Eq. (14) to evaluate thermal conductivity [48]

Nanoparticle	Aspect ratio	C_k^{shape}	$C_k^{surface}$	C_k
Platelet	1:0.125	5.72	-3.11	2.61
Brick	1:1:1	3.72	-0.35	3.37
Blade	1:6:0.08334	8.26	-5.52	2.74
Cylinder	1:8	4.82	-0.87	3.95

Table 5 Values for parameters used in Eq. (15) to estimate viscosity [48]

Constant	Platelet	Brick	Blade	Cylinder
A_1	37.10	1.90	14.60	13.50
A_2	612.60	471.40	123.30	904.40

Table 6 Applied constants used to estimate thermophysical properties of oblate-spheroid nanoparticles in the present work [49]

Particle	Ψ	δ	φ_m
Oblate-spheroid	0.4904	0.13	0.575

Table 7 Thermophysical properties for boehmite nanoparticles and water-ethylene glycol base fluid at 298 K [35]

	$\lambda/\text{Wm}^{-1}\text{K}^{-1}$	μ/Pas	$C_{np}/\text{Jkg}^{-1}\text{K}^{-1}$	ρ/kgm^{-3}
$\gamma - \text{AlO}(\text{OH})$	30	-	618.30	3050.00
$\text{H}_2\text{O} - \text{EG}$	0.3799	0.00339	3300.00	1067.50

$$\frac{\lambda_{nf}}{\lambda_f} = \left(\frac{(\lambda_{np} + (n - 1)\lambda_f - (n - 1)(\lambda_f - \lambda_{np}))\varphi}{(\lambda_{np} + (n - 1)\lambda_f + (\lambda_f - \lambda_{np}))\varphi} \right) \tag{16}$$

$$\frac{\mu_{nf}}{\mu_f} = \left(1 - \frac{\varphi}{\varphi_m} \right)^{-2} \tag{17}$$

where subscript np denotes the boehmite nanoparticles, and $n = \frac{3}{\Psi}$ refers to the shape factor. The values of Ψ and φ_m for the oblate-spheroid nanoparticles are presented in Table 6. The value of φ_m which is empirically found depends on the geometric property $\delta = \frac{c}{a}$, as represented in Fig. 3. In addition, the thermophysical properties of $\gamma - \text{AlO}(\text{OH})$ nanoparticles and water-ethylene glycol (50:50) are provided in Table 7.

Furthermore, it has been shown that nanofluid's density and specific heat capacity are not sensitive to the nanoparticle's shape. Accordingly, the density and the constant

pressure-specific heat capacity for the aforesaid shapes are estimated using Eqs. (18 and 19).

$$\rho_{nf} = (1 - \varphi)\rho_f + \varphi\rho_{np} \quad (18)$$

$$C_{p_{nf}} = \frac{(1 - \varphi)\rho_f C_{p_f} + \varphi\rho_{np} C_{p_{np}}}{\rho_{nf}} \quad (19)$$

Performance indices

The inlet velocity is estimated from the prescribed Re as

$$u_{in} = \frac{Re \mu_{nf}}{\rho_{nf} D_h} \quad (20)$$

To address the thermal–hydraulic performance of the nanofluid, the dimensionless parameters, particularly, the friction factor and the surface average Nusselt number (Nu), are used. Both are defined as follows:

$$f = \frac{2D_h \Delta p}{\rho_{nf} u_{mean}^2 L} \quad (21)$$

$$Nu = \frac{q'' D_h}{(T_{wall} - T_{bulk}) \lambda_{nf}} \quad (22)$$

where T_{bulk} is evaluated as follows:

$$T_{bulk} = 0.5(T_{in} + T_{out}) \quad (23)$$

The thermo-hydraulic performance evaluation criterion due to the presence of wire-coil insert is expressed in terms of (PEC_{geo}), which is calculated as follows:

$$PEC_{geo} = \frac{\left(\frac{Nu_{in}}{Nu_{em}}\right)}{\left(\frac{fr_{in}}{fr_{em}}\right)^{1/3}} \quad (24)$$

where subscripts (in and em) connote channels with CWI and empty channel, respectively.

The corresponding thermo-hydraulic performance evaluation criteria due to the usage of nanofluid is announced through (PEC_{nf}), which is defined as follows:

$$PEC_{nf} = \frac{\left(\frac{Nu_{nf}}{Nu_f}\right)}{\left(\frac{fr_{nf}}{fr_f}\right)^{1/3}} \quad (25)$$

where subscripts (nf and f) connote nanofluid and base fluid, respectively.

The normalized friction factor (fr^G) and the surface average Nusselt number (Nu^G) due to geometry modifications are also defined as follows:

$$fr^G = \frac{fr_{in}}{fr_{em}} \quad (26)$$

$$Nu^G = \frac{Nu_{in}}{Nu_{em}} \quad (27)$$

While the corresponding normalized friction factor (fr^N) and the surface average Nusselt number (Nu^N) due to the usage of nanofluid are delineated with

$$fr^N = \frac{fr_{nf}}{fr_f} \quad (28)$$

$$Nu^N = \frac{Nu_{nf}}{Nu_f} \quad (29)$$

Computational model development, grid sensitivity, and validation

The entire 3D domain for squared channels with and without CWIs has been generated based on the polyhedron finite mesh technique. Enhanced wall treatment technique was applied for near-wall modeling to satisfy the desirable value ($y^+ \approx 1$), such that a small mesh size was used near the wall of the channel, and the surface of CWI, as shown in Fig. 4. This has been done in order to apprehend the boundary layer effect while a coarser mesh was used in the core fluid region. The governing equations (continuity, momentum, and energy) and the turbulence equations have been solved using the finite volume method through ANSYS Fluent® [50]. The imposed boundary conditions are shown in Fig. 1a and summarized in Table 3.

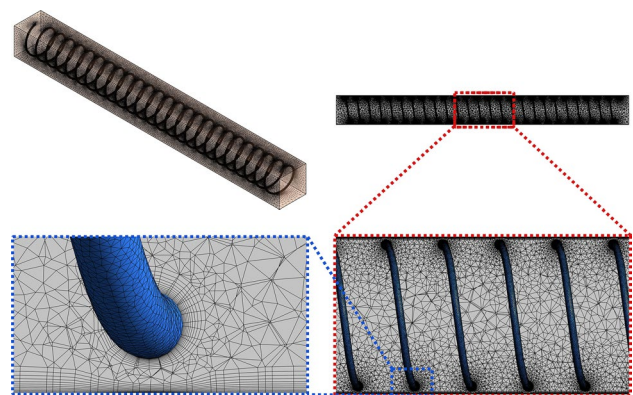


Fig. 4 Mesh generation for channel fitted with circular CWI

Semi-implicit pressure link equation (SIMPLE algorithm) was employed for coupling pressure and velocity equations. The momentum, energy, turbulent kinetic energy generation (k), and its rate of dissipation (ϵ) equations were discretized using second-order upwind scheme, while the resulting algebraic equations were solved using the iterative method. The convergence criteria for all equations were set to 10^{-6} such that

$$\left| \frac{\Gamma^{k+1} - \Gamma^k}{\Gamma^{k+1}} \right| \leq 10^{-6} \tag{30}$$

where k and Γ denote iteration number and field variables, respectively. Grid sensitivity analysis of the model was performed by estimating the Nu and fr for distilled water flowing through a square channel provided with a circular CWI. The variation of Nu and fr against the number of grids is shown in Fig. 5a. In order to reduce computational time without compromising the accuracy of the results, the mesh configuration of 5.137×10^6 was chosen and used for the entire models. Also, the results of the grid sensitivity test in terms of local Nusselt number and pressure for coarse, fine, and finest generated grid are shown in Fig. 5b–c. The reliability of this model was further validated by estimating the Nu and fr of distilled water in an empty square duct across a range of Re. The obtained values for Nu were compared with existing empirical correlations (Appendix A) by Dittus–Boelter [51], Sieder and Tate [52], and Gnielinski [53], while the values of fr have been compared with Petukhov [54], Blasius [55], and Filonenko [56] correlations as shown in Fig. 6a–b. It could be seen that a good agreement exists between the estimated values and their corresponding correlations. For instance, the average percentage deviation of estimated Nu relative to Dittus–Boelter, Sieder and Tate, and Gnielinski correlations is 6.63, 1.57, and 5.40%, respectively. The average percentage deviation of fr estimated relative to Petukhov,

Blasius, and Filonenko correlation is 3.28, 4.48, and 3.26%, respectively. For more robust of the model, another validation with experimental results of nanofluid flow in circular duct in terms of local Nusselt number $Nu(x)$ investigated by Hafiz [57]. The average deviation between the present model and the experimental results is 7.12%, as shown in Fig. 6c. Consequently, the present model is reliable and can be used in the rest of cases.

Results and discussion

This section provides and discusses simulation results for the turbulent thermo-hydraulic performance of $\gamma - \text{AlO}(\text{OH})/\text{H}_2\text{O} - \text{EG}$ nanofluid, prepared from previously described nanoparticles and flowing through a square duct with various CWIs. In summary, there are an empty channel and seven other designs, all simulated at six values of Re, for five different nanofluids (each with VR = 2 and 4%) and a base fluid (VR = 0%) for comparison; which means 528 simulated cases. Sect. "Hydrodynamic performance" examines the effect of nanoparticle shapes, nanoparticle volume ratio ($0 \leq \phi \leq 4\%$), Re ($5.0 \times 10^3 \leq \text{Re} \leq 4.0 \times 10^4$), and geometries of CWI on hydrodynamics. Sect. "Heat transfer performance" examines the effect of the aforementioned terms on heat transfer performance, while Sect. "Thermo-hydraulic performance" discusses the thermo-hydraulic performance criterion.

Hydrodynamic performance

Figure 7a shows the contour of the planar view of TKE for nanofluid flow with platelet nanoparticles in the duct fitted with various CWIs at $\text{Re} = 5.0 \times 10^3 - \phi = 4\%$. This term

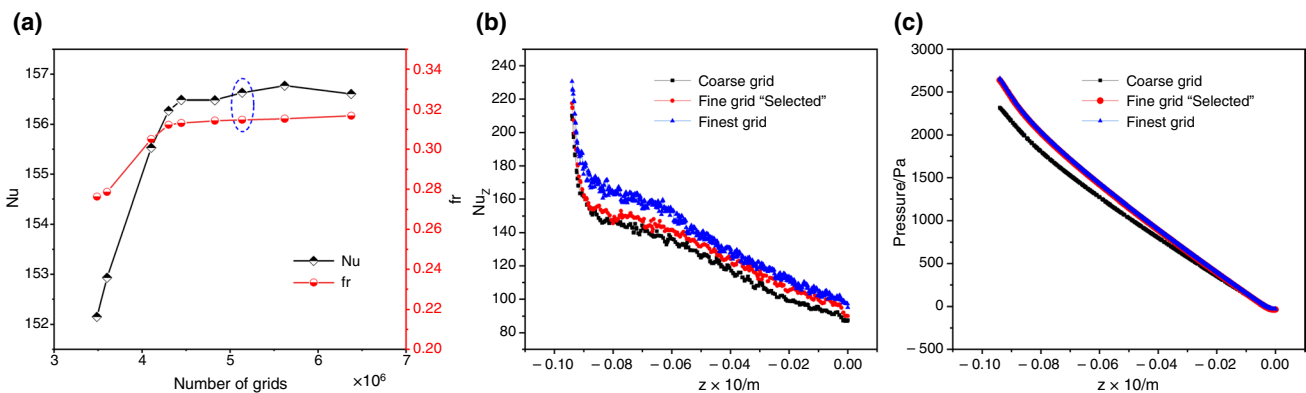


Fig. 5 a Results of grid sensitivity test in terms of average Nusselt number and friction factor (The selected mesh size is marked with the blue elliptic shape). b Results of grid sensitivity test in terms of local

Nusselt number for coarse, fine, and finest generated grids. c Results of grid sensitivity test in terms of local pressure for coarse, fine, and finest generated grids

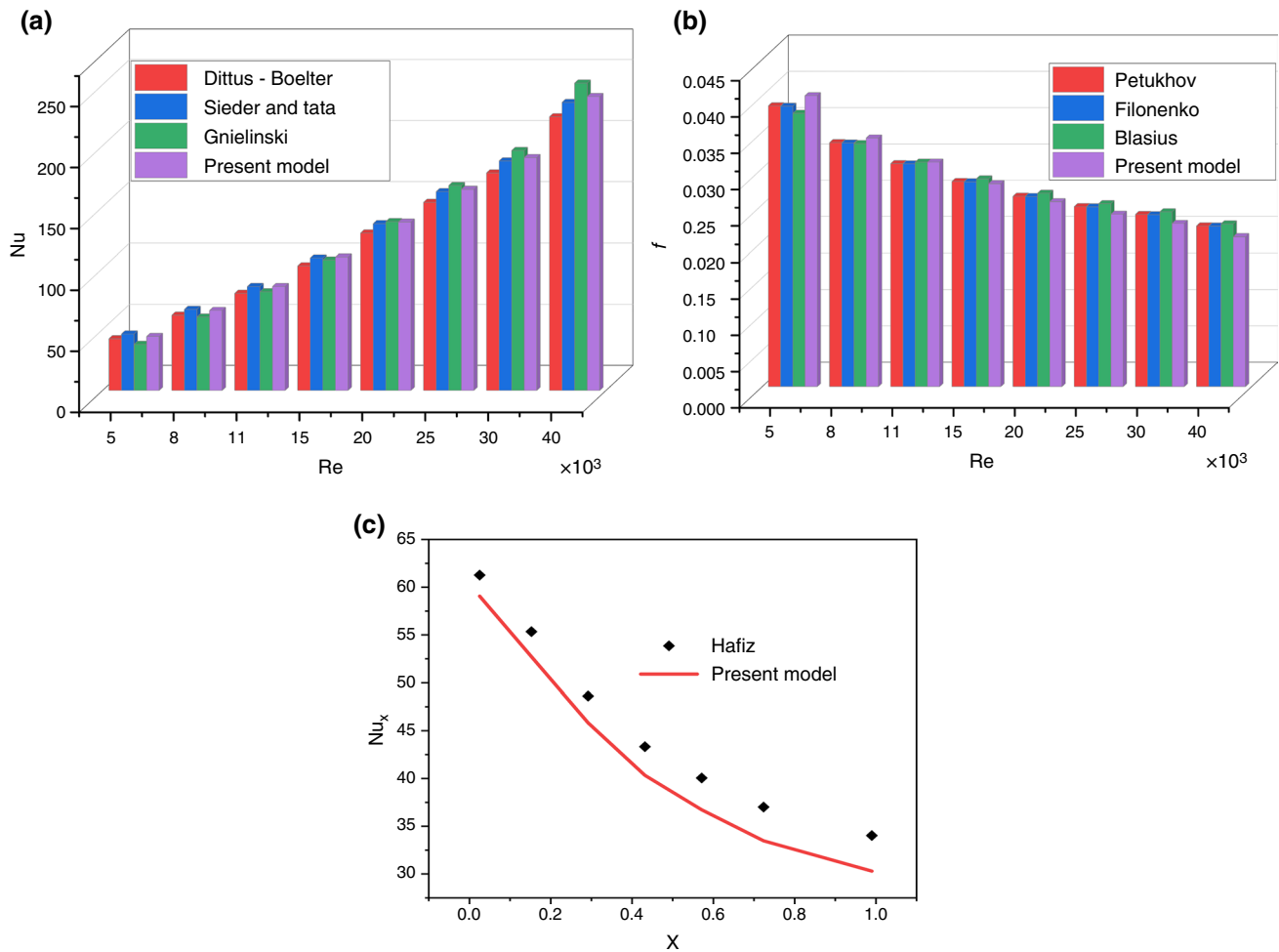


Fig. 6 **a** Validation of the present model against experimental correlations in terms of Nu. **b** Validation of present model against experimental correlations in terms of f . **c** Validation of present model against experimental results by Hafiz [57] in terms of local Nusselt number $Nu(x)$

is essential to investigate hydrodynamic and heat transfer performance in a thermal system as it measures the intensity at which fluid at the viscous sublayer is being mixed with fluid at the core fluid zone. From the figure, it is evident that TKE is higher in ducts fitted with CWIs than in empty ducts. Furthermore, high intensity of TKE is noticed near the CWI surface. This result is expected as the presence of CWI in the duct induces secondary flow in the core region, resulting in high-flow velocity fluctuations. The high intensity noticed near the wall of CWI is attributed to the high disturbance of the radial and tangential velocities of the fluid near the CWI by the vortex of the secondary flow. This leads to high fluctuation of the velocity near the wire's surface. A higher pressure drop accompanies this process. It should be noticed that the high TKE observed in channel designs contributes to the improvement of CHTP by increasing the rate of mixing between hot fluid zones near the wall and cold fluid zones, which also decreases the thickness of the thermal boundary layer (δ_{th}). Figure 7b reveals the distribution of TKE in

nanofluid prepared from various nanoparticle shapes flowing in the duct fitted with the square CWI of various nanoparticle shapes at $Re = 5.0 \times 10^3 - \phi = 4\%$. A significant value of TKE is announced near the wall of the ducts which is attributed to the previously indicated velocity fluctuation. Furthermore, it is shown that TKE is higher in nanofluid than base fluid except in oblate-spheroid. Additionally, it can be seen that the nanofluid prepared from platelet nanoparticles has the highest TKE among the nanofluids considered. This high TKE is due to the relatively high viscosity of the platelet nanofluid. It shall be emphasized that high viscosity will be counterbalanced with the high inlet velocity since we operate at constant Re. Later on, the reason for the high viscosity of nanofluid made from platelet nanoparticles will be explained. Figure 8a depicts the variation of fr for all nanofluids against Re for aforesaid channel configurations. It is clear that fr decreases as Re increases for multiple duct configurations considered. Whereas shown, across the range of Re considered ($5.0 \times 10^3 \leq Re \leq 4.0 \times 10^4$), the values of

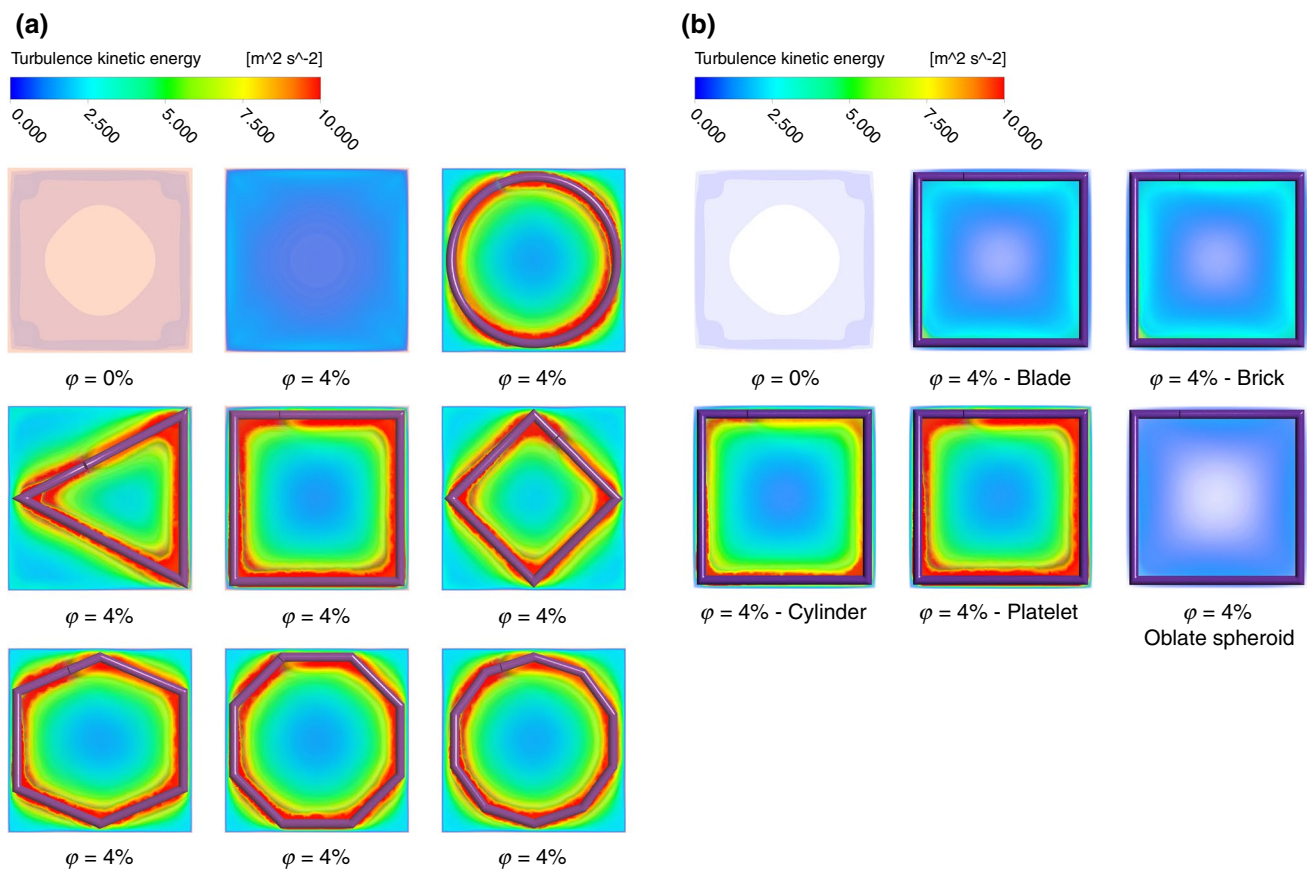


Fig. 7 **a** Contour of local TKE for nanofluid flow with platelet nanoparticles in the duct fitted with various CWIs at $Re=5000-\phi = 4\%$. **b** Contour of local TKE in the duct fitted with square CWI of various nanoparticle shapes at $Re=5000-\phi = 4\%$

fr for channels fitted with circular, triangular, square, square-diamond, hexagon, octagon, and decagon wires decrease by 38.52, 42.02, 38.82, 44.41, 38.62, 37.15, and 40.23%, respectively. While the corresponding percentage reduction for empty ducts is 48.54%. This result is expected as an increase in Re in the turbulent flow regime reduces the thickness of the viscous sublayer. Figure 8b shows the variation of fr^G against Re . As represented before, it could be seen that the empty square duct has the lowest fr compared with ducts with CWI. For instance, at $Re = 1.5 \times 10^4$, the values of fr^G in channels fitted with circular, triangular, square, square-diamond, hexagon, octagon, and decagon wire are 11.28, 11.57, 10.52, 11.70, 12.01, 11.28, and 11.93, respectively.

The relatively high values of fr^G observed for the duct with CWI are attributed to the following factors: (i) high shear stress and pressure drag created by the presence of the CWI, (ii) constriction of the flow passage due to the presence of CWI, (iii) the adverse pressure drop (APG) which result in flow recirculation, and (iv) swirl flow induced by the interaction between the flow and the coil, boundary layer separation, and reattachment. These factors contributed to the increase in pressure drop and consequently fr in the duct

with CWI. For instance, the swirl flow increases the flow turbulence, the constriction of the flow passage increases the flow's velocity, and the accelerated fluid increases the flow resistance. Lastly, the APG increases the pressure drop within the channel. The implication of high fr^G is that high pumping power will be required in the operating channel with CWI. Also, it is explicit that among various CWIs examined, duct with square CWI has relatively lowest fr^G , while duct with hexagonal one has the highest value. The low value observed for duct fitted with square CWI is associated with its geometry similarity with the outer duct. Lastly, the values of fr^G increase as Re increases for all channel designs. For example, at $Re = 5.0 \times 10^3$, the values of fr^G are 10.27, 10.84, 9.42, 11.14, 10.91, 10.20, and 10.97 in circular, triangular, square, square-diamond, hexagon, octagon, and decagon wire shapes, respectively. While the corresponding values at $Re = 4.0 \times 10^4$ are 12.27, 12.21, 11.57, 12.03, 13.01, 12.46, and 12.74, respectively. This high value of fr^G is attributed to an abnormal rise in shear stress, pressure drag, swirl flow, and APG as Re increases.

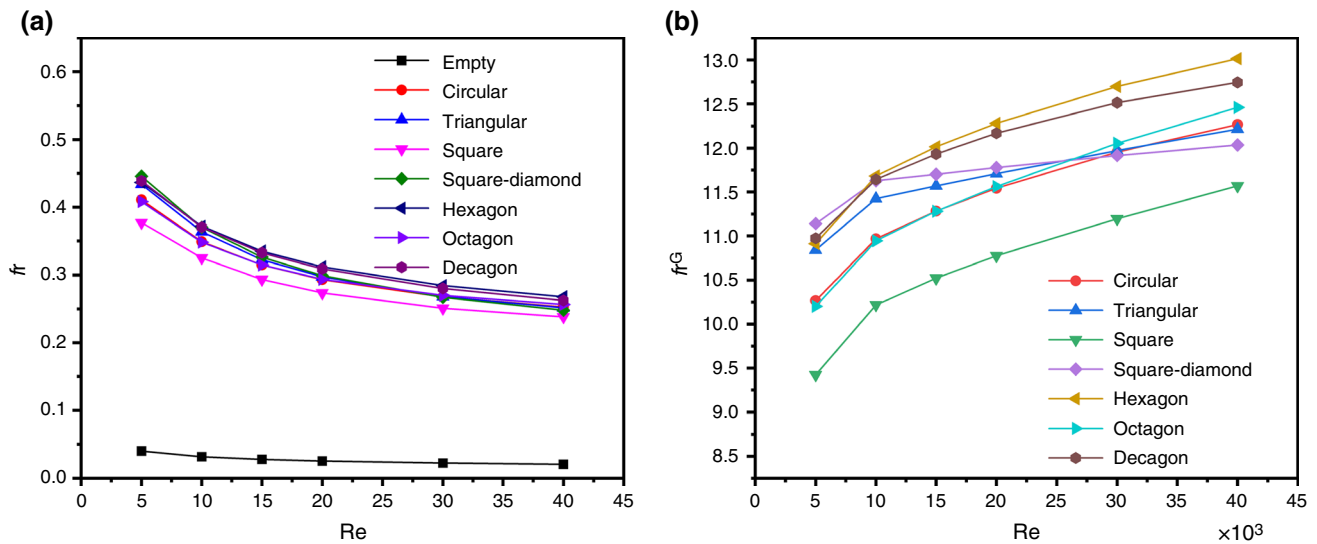


Fig. 8 **a** Variation of global friction factor against Re for empty duct and all other configurations of fitted CWIs ($\varphi = 4\%$). **b** Variation of normalized friction factor against Re for the various CWIs compared to the empty one ($\varphi = 4\%$)

Heat transfer performance

The temperature contours shown in Fig. 9 illustrate the effect of using platelet nanofluid flow ($VR = 4\%$) within our previously described channels, by presenting the temperature distribution along the axial flow direction. It could be seen that the presence of the CWI undermined the development of the thermal boundary layer (TBL), which leads to enhancement in CHTP. Also, we noticed that temperature distribution is relatively uniform in the channel with CWI compared with empty one. This result is attributed to high turbulence induced by the presence of CWI in the channel. The high turbulence increases the rate of mixing rate of hot fluid near the wall with cold fluid at the core region. This reduces the temperature gradient of the fluid. Furthermore, it was noticed that the thickness of the thermal boundary layer (δ_{th}) in base fluid (water–ethylene glycol) is bigger compared with $\gamma - \text{AlO}(\text{OH})/\text{H}_2\text{O} - \text{EG}$ nanofluid. This implies that the nanofluid enhances CHTP compared with base fluid. Also, it shall be noted that the thinner the δ_{th} around a hot solid object the higher the rate of CHTP to the surrounding fluid.

Figure 10a shows the variation of Nu for $\gamma - \text{AlO}(\text{OH})/\text{H}_2\text{O} - \text{EG}$ nanofluid in empty and other seven designed channels against Re . It is observed that wire-fitted channels always outperform the empty duct in terms of Nu at the same Re . For instance, at $Re = 1.5 \times 10^4$, the values of Nu for blade nanofluid ($VR = 2\%$) flowing inside the channel fitted with CWI (circular, triangular, square, square-diamond, hexagon, octagon, and decagon) are 295.82, 312.35, 323.08, 310.71, 306.48, 313.32, and 291.67, respectively. The corresponding value of Nu in the

empty one is 201.26. This remarkable thermal enhancement is associated with the existence of CWI which (i) interrupts the development of the thermal boundary layer, (ii) produces swirl flow that induces tangential velocity component, which consequently enhances the rate of mixing of hot fluid near the wall with the accelerated core fluid [12, 26], (iii) reduces the cross section of the flow field which leads to high advection heat transfer that eventually enhances CHTP, (iv) produces APG which induces secondary flow, and (v) produces longitudinal vortices which also enhances the mixing rate. Also, it is obvious that an increase in Re enhances Nu . For example, across the range of Re considered ($5.0 \times 10^3 \leq Re \leq 4.0 \times 10^4$), the values of Nu for blade nanofluid ($VR = 2\%$) for the same aforementioned channel designs increase by factor of 4.02, 4.02, 2.61, 4.57, 3.73, 3.42, and 4.43, respectively. The corresponding factor in empty duct is 5.74. The increment is attributed to decrease in δ_{th} as Re increases, ($\delta_{th} \propto \frac{1}{Re^{0.2}}$) [32]. The variation of Nu^G against Re for the various channel designs is depicted in Fig. 10b. As demonstrated in the figure, the enhancement of Nu archived through CWI, compared to an empty channel, diminishes as Re increases. For instance, when the previously mentioned channel configurations are operating at $Re = 5.0 \times 10^3$, the values of Nu^G for blade nanofluid ($VR = 2\%$) are 1.94, 1.97, 2.64, 1.84, 2.09, 2.24, and 1.79, respectively. While that, at $Re = 4.0 \times 10^4$, the corresponding values are 1.36, 1.38, 1.20, 1.47, 1.36, 1.33, and 1.39, respectively. This result shows that as Re increases, the effect of formation factors (reduction in thickness of TBL, swirl flow, contraction of the flow passage, turbulence, and secondary flow) that

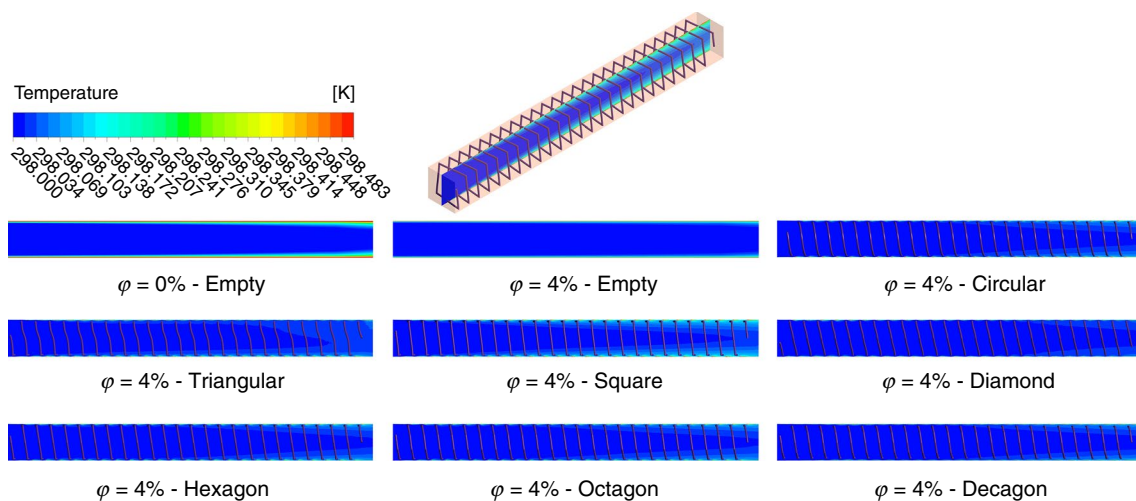


Fig. 9 Lateral views of temperature distribution for platelet nanofluid flow ($Re = 5000 - \phi = 4\%$) in various channel designs

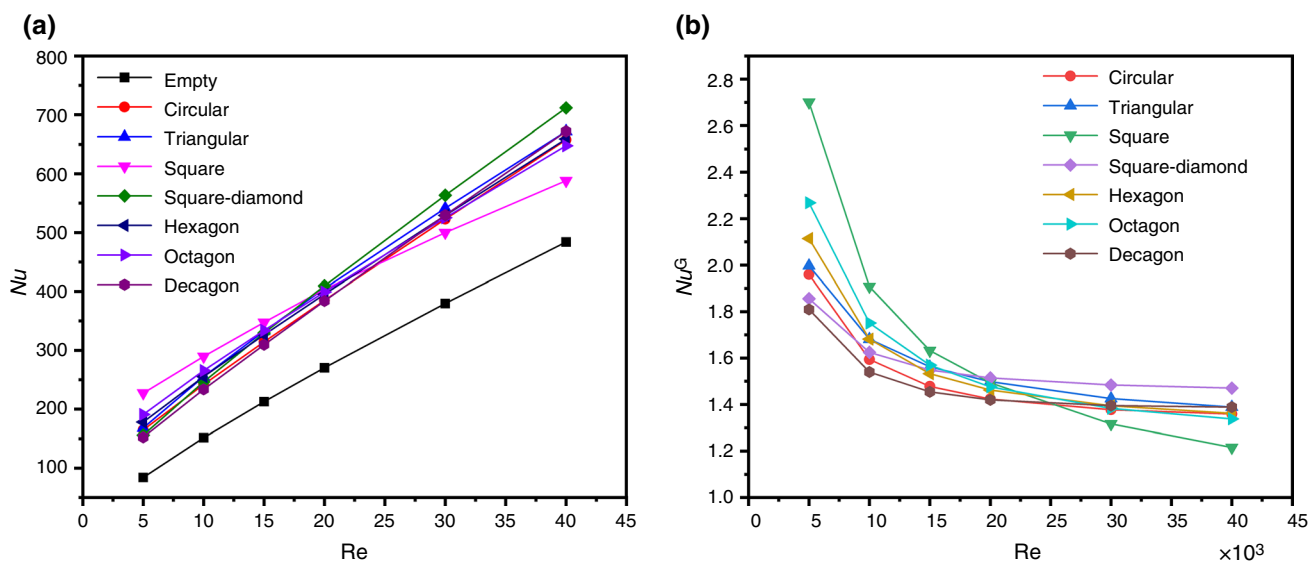


Fig. 10 **a** Variation of Nusselt number against Re for empty duct and all other configurations of fitted CWIs ($\phi = 4\%$). **b** Variation of normalized Nusselt number against Re for the various CWIs compared to the empty one ($\phi = 4\%$)

contribute to the enhancement of CHTP in the channel with CWI began to wane. In other words, the high-flow rate mainly dominates the thermal enhancement over the other thermal improvement parameters. Back to Fig. 10b, it is noted that at low Re ($Re = 5 \times 10^3$), duct with square CWI configuration has the highest value for Nu^G , while the square-diamond wire-fitted channel has the lowest. However, the opposite is the case at high Re ($Re = 4.0 \times 10^4$). Hence, provided that dP is not an issue, duct with square CWI is advantageous at low Re, while at a high-flow rate switching to a square-diamond design is better. On the other hand, the impact of boehmite-to-water–ethylene glycol VRs on the thermal performance of

different nanoparticle shapes used in the present exploration is displayed in Fig. 11. Figure 11a–b better illustrates the variation of λ_{nf} and μ_{nf} for $\gamma - AlO(OH)/H_2O - EG$ nanofluids with nanoparticle VRs. It is evident that the augmentation of nanoparticle VR elevates the magnitudes of the two quantities. For instance, across the range of nanoparticle VR examined ($0.0 \leq \phi \leq 0.04$), the λ_{nf} prepared from platelet, blade, cylinder, brick, and oblate-spheroid nanoparticles increase by a factor of 1.10, 1.11, 1.16, 1.13, and 1.24, respectively. The corresponding increase in μ_{nf} is 3.46, 1.78, 2.99, 1.83, and 1.16, respectively. Moreover, it is perceived that nanofluid prepared from oblate-spheroid nanoparticles has the highest λ_{nf} ,

while platelet nanofluid has the lowest. Regarding μ_{nf} , the opposite is achieved. The high μ_{nf} of nanofluid with platelet nanoparticles is attributed to its relatively small size compared to other shapes considered. This small size allows more nanoparticles to be packed into the base fluid, which invariably improves μ_{nf} . The variation of Prandtl number (Pr) for nanofluids prepared from various nanoparticle shapes against their volume concentrations is demonstrated in Fig. 11c. It is clear that platelet nanofluid has a maximum value of Pr, while nanofluid prepared from oblate-spheroid nanoparticles has the minimum. This high Pr of platelet shape is associated with its relatively high μ_{nf} and low λ_{nf} , whereas all nanofluids have the same density and specific heat capacity.

The influence of nanoparticle shapes on Nu^N is shown in Fig. 11d. It is explicit that the Nu^N is maximum for platelet nanofluid and minimum for oblate-spheroid nanofluid. For instance, across the range of VR considered ($0 \leq \varphi \leq 4\%$) and while the empty channel is operating at $Re = 5.0 \times 10^3$, the percentage enhancements of Nu^N for platelet, blade, cylinder, brick, and oblate-spheroid nanofluids are 35.37, 11.96, 28.19, 12.12, and -4.66% , respectively. The high Nu^N achieved for nanofluid prepared from platelet nanoparticles is attributed to its high Pr, and the increment is attributed to increase in μ_{nf} and λ_{nf} as φ increases. It shall be noted that increase in the former leads to high inlet velocity since we are operating at constant Re, and an increase in the latter leads to high heat transfer performance.

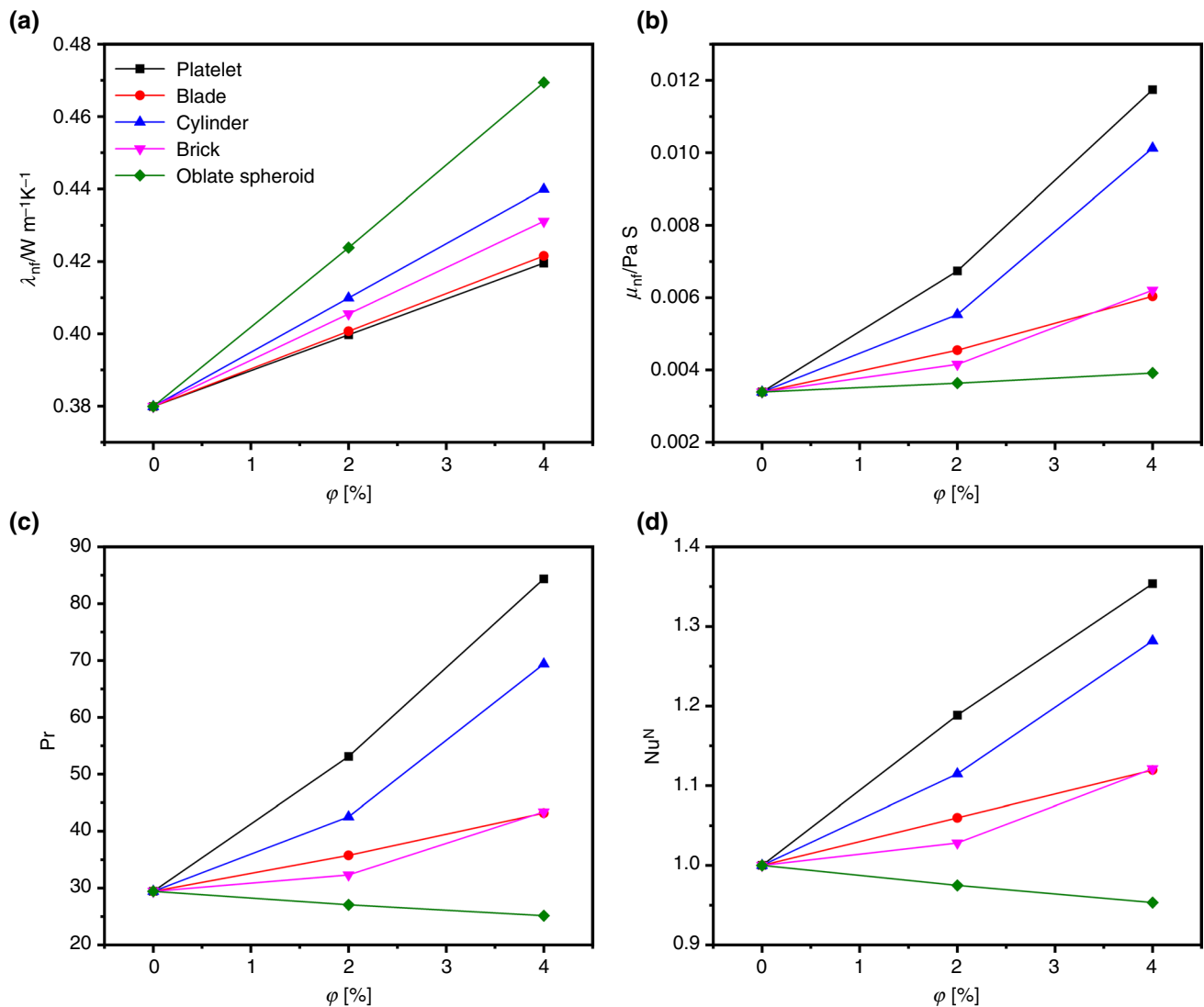


Fig. 11 **a** Variation of thermal conductivity, **b** Dynamic viscosity, **c** Prandtl number, and **d** Normalized average Nusselt number for empty channel at $Re = 5 \times 10^3$ for various nanofluids shapes against nanoparticle volume ratios

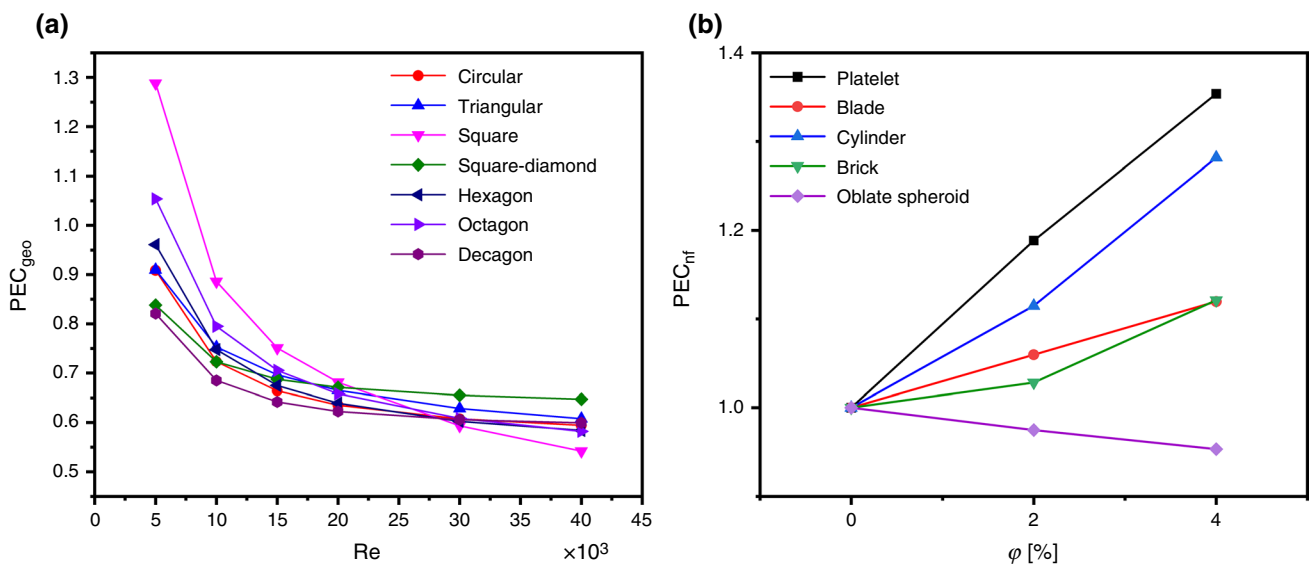


Fig. 12 a Variation of PEC_{geo} for blade nanofluid ($\varphi = 4\%$) against Re . b Variation of PEC_{nf} for various nanofluids shape against nanoparticle volume ratios while empty duct at $Re = 5000$

Thermo-hydraulic performance

Figure 12a maps the variation of PEC_{geo} of $\gamma - AlO(OH)/H_2O - EG$ nanofluid prepared from blade nanoparticles ($\varphi = 4\%$) against Re for all simulated duct configurations. Driven by exceptional thermal and hydrodynamic performance, the channels with square and octagon CWIs have a value of PEC_{geo} greater than unity at low Re ($Re = 5.0 \times 10^3$), while for other configurations, the values are lower than unity across the entire Re range ($5.0 \times 10^3 \leq Re \leq 4.0 \times 10^4$). This implies that if it is taken into consideration enhancement in convective heat transfer and dP due to existence of turbulators, only square and octagon wire-fitted channels have more favorable energy performance, and they allow for operating at a low-flow rate ($Re = 5.0 \times 10^3$) while surpassing the performance of an empty channel. Beyond this Re , there is no enhancement in the overall thermal-hydraulic performance for all channel designs. This is attributed to the fact that at $Re = 5.0 \times 10^3$, enhancement in average surface Nu obtained for both configurations (square and octagon CWIs) is accompanied by a moderate increase in dP while the enhancement in Nu observed for other designs at higher Re ($Re > 5.0 \times 10^3$) is accompanied with high increase in dP . Of course, this remark assumes that hydrodynamic performance is as important as CHTP. Otherwise, significant improvements in CHTP are easily achieved with various channel designs used in the present work. Also, it is notable that as Re increases the values of PEC_{geo} decreases. For instance, while using cylinder nanofluid ($VR = 2\%$) across the aforementioned entire range of Re , the values of PEC_{geo} for ducts provided with

circular, triangular, square, square-diamond, hexagon, octagon, and decagon CWIs decrease by 34.59, 33.16, 57.92, 22.75, 39.22, 44.75, and 26.96%, respectively. This result is expected as Nu^G decreases as Re increases while fr^G increases as Re increases. To examine the influence of nanoparticle shapes on the overall energetic performance, Fig. 12b shows the variation in PEC_{nf} . It can be seen that while the empty channel is operating at $Re = 5.0 \times 10^3$, nanofluid prepared from platelet, cylinder, brick, and blade nanoparticles has values of PEC_{nf} that is greater than unity. This implies that the usage of these nanofluids is proven to be an energy-efficient solution compared with base fluid (water-ethylene glycol). Furthermore, according to the previously mentioned operating condition and across the range of nanoparticle VR considered ($0 \leq \varphi \leq 4\%$), the percentage improvements of PEC_{nf} for platelet, blade, cylinder, brick, and oblate-spheroid boehmite/water-ethylene glycol are 35.37, 11.96, 28.19, 12.12, and -4.66% , respectively.

Conclusions

This study examined the turbulent heat transfer performance of nanofluid [$(\gamma - AlO(OH))/water-ethylene glycol (50:50)$] prepared from various nanoparticle shapes (blade, brick, cylinder, oblate-spheroid, and platelet), which flows through a square duct fitted with CWI of various geometries (circular, triangular, square, square-diamond, hexagon, octagon, and decagon). The channel is subject to a uniform external heat flux, a well-validated computational model has been

developed to capture the hydrothermal characteristics in the duct when changing the fitted CWI configurations, nanoparticle's shape, and volume ratio (VR). Some of the main findings of this study are as follows:

1. The presence of CWI in the channel enhances CHTP. When blade nanofluid ($\varphi = 2\%$) is at a minimum flow rate ($Re = 5.0 \times 10^3$), the normalized (Nu^G) for duct provided with CWI (circular, triangular, square, square-diamond, hexagon, octagon, and decagon) is 1.94, 1.97, 2.64, 1.84, 2.09, 2.24, and 1.79, respectively.
2. The increase in Re enhances CHTP for all channel configurations considered. Across the range of Re considered ($5.0 \times 10^3 \leq Re \leq 4.0 \times 10^4$), the Nu for blade nanofluid ($\varphi = 2\%$) flowing through the same aforementioned channel designs increases by a factor of 4.02, 4.02, 2.61, 4.57, 3.73, 3.42, and 4.43, respectively.
3. Among the various shapes of nanoparticles considered, it was found that nanofluid prepared from platelet nanoparticles has the best thermal performance while oblate-spheroid nanofluid has the minimum Nu . At the lowest Re , the Nu for platelet, blade, cylinder, brick, and oblate-spheroid boehmite/water–ethylene glycol nanofluids flowing through the empty channel is 89.31, 79.62, 83.77, 77.27, and 73.26, respectively, for $\varphi = 2\%$.
4. The wire-fitted channels have higher fr compared with the empty channel. At $Re = 5.0 \times 10^3$, the normalized (fr^G) assigns to 10.27, 10.84, 9.42, 11.14, 10.91, 10.20, and 10.97, respectively, while using blade nanofluid ($\varphi = 2\%$) for the same design order as described above.
5. The channels with square and octagon CW configurations are better than empty channel at low Re ($PEC_{geo} > 1$). However, at high Re , neither of them perform very well ($PEC_{geo} < 1$).
6. The increase in Re decreases PEC_{geo} . Across the afore-said range of Re , the PEC_{geo} for channels provided with circular, triangular, square, square-diamond, hexagon, octagon, and decagon CWI decreases by 34.59, 33.16, 57.92, 22.75, 39.22, 44.75, and 26.96%, respectively, while using cylinder nanofluid ($\varphi = 2\%$).
7. In terms of PEC_{nf} , all nanofluids prepared from various nanoparticle shapes are better compared with base fluid (boehmite/water–ethylene glycol (50:50)), except the one prepared from oblate-spheroid nanoparticles.
8. The increase in nanoparticle φ enhances PEC_{nf} . When the empty channel is operating at $Re = 5.0 \times 10^3$, the PEC_{nf} for platelet, blade, cylinder, brick, and oblate-spheroid boehmite/water–ethylene glycol nanofluids increases by 35.37, 11.96, 28.19, 12.12, and -4.66% , respectively.

Appendix

Appendix A: Correlations used for model validation

Dittus–Boelter [51]:

$$Nu = 0.023Re^{0.8}Pr^{0.4}; 0.6 \leq Pr \leq 160; Re \geq 10^4 \quad (31)$$

Sieder and Tate [52]:

$$Nu = 0.027Re^{0.8}Pr^{0.33} \left(\frac{\mu}{\mu_w} \right)^{0.14}; 0.7 \leq Pr \leq 16700; Re \geq 10^4 \quad (32)$$

Gnielinski [53]:

$$Nu = 0.012(Re^{0.87} - 280)Pr^{0.4}; 1.5 \leq Pr \leq 500; 3000 \leq Re \leq 10^5 \quad (33)$$

Petukhov [54]:

$$f = (0.79 \ln Re - 1.64)^{-2}; 3,000 \leq Re \leq 5 \times 10^6 \quad (34)$$

Blasius [55]:

$$f = 0.316Re^{-0.25}; 3000 \leq Re \leq 2 \times 10^4 \quad (35)$$

$$f = 0.184Re^{-0.25}; Re \geq 2 \times 10^4 \quad (36)$$

Filonenko [56]:

$$f = (1.82 \log Re - 1.64)^{-2}; 2300 < Re < 10^6 \quad (37)$$

Funding Open access funding provided by The Science, Technology & Innovation Funding Authority (STDF) in cooperation with The Egyptian Knowledge Bank (EKB).

Open Access This article is licensed under a Creative Commons Attribution 4.0 International License, which permits use, sharing, adaptation, distribution and reproduction in any medium or format, as long as you give appropriate credit to the original author(s) and the source, provide a link to the Creative Commons licence, and indicate if changes were made. The images or other third party material in this article are included in the article's Creative Commons licence, unless indicated otherwise in a credit line to the material. If material is not included in the article's Creative Commons licence and your intended use is not permitted by statutory regulation or exceeds the permitted use, you will need to obtain permission directly from the copyright holder. To view a copy of this licence, visit <http://creativecommons.org/licenses/by/4.0/>.

References

1. Kaood A, Abou-Deif T, Eltahan H, Yehia MA, Khalil EE. Numerical investigation of heat transfer and friction characteristics for turbulent flow in various corrugated tubes. Proc Inst Mech Eng Part A J Power Energy. 2019;233:457–75.

2. Fadodun OG, Amosun AA, Okoli NL, Olaloye DO, Ogundeji JA, Durodola SS. Numerical investigation of entropy production in SWCNT/H₂O nanofluid flowing through inwardly corrugated tube in turbulent flow regime. *J Therm Anal Calorim.* 2021;144:1451–66.
3. Kaood A, Abubakr M, Al-Oran O, Hassan MA. Performance analysis and particle swarm optimization of molten salt-based nanofluids in parabolic trough concentrators. *Renew Energy.* 2021;177:1045–62.
4. Fadodun OG, Kaood A, Hassan MA. Investigation of the entropy production rate of ferrosferric oxide/water nanofluid in outward corrugated pipes using a two-phase mixture model. *Int J Therm Sci.* 2022;178:107598.
5. Kaood A, Hassan MA. Thermo-hydraulic performance of nanofluids flow in various internally corrugated tubes. *Chem Eng Process Intensif.* 2020;154: 108043.
6. Kaood A, Abou-Deif T, Eltahan H, Yehia MA, Khalil EE. Investigation of thermal-hydraulic performance of turbulent flow in corrugated tubes. *J Eng Appl Sci.* 2018;65:307–29.
7. Hashemian M, Jafarmadar S, El-Shorbagy MA, Rahman AA, Dahari M, Wae-hayee M. Efficient heat extraction from the storage zone of solar pond by structurally improved spiral pipes; numerical simulation/experimental validation. *Energy Rep.* 2022;8:7386–400.
8. Hassan MA, Kassem MA, Kaood A. Numerical investigation and multi-criteria optimization of the thermal-hydraulic characteristics of turbulent flow in conical tubes fitted with twisted tape insert. *J Therm Anal Calorim* 2021.
9. Kaood A, Fadodun OG. Numerical investigation of turbulent entropy production rate in conical tubes fitted with a twisted-tape insert. *Int Commun Heat Mass Transf.* 2022;139:106520.
10. Kaood A, Aboulmagd A, Othman H, ElDegwy A. Numerical investigation of the thermal-hydraulic characteristics of turbulent flow in conical tubes with dimples. *Case Stud Therm Eng.* 2022;36: 102166.
11. Khalil EE, Kaood A. Numerical investigation of thermal-hydraulic characteristics for turbulent nanofluid flow in various conical double pipe heat exchangers. In *AIAA Scitech 2021 Forum*. Reston, Virginia: American Institute of Aeronautics and Astronautics; 2021. p. 1–21
12. Keklikcioglu O, Ozceyhan V. Experimental investigation on heat transfer enhancement of a tube with coiled-wire inserts installed with a separation from the tube wall. *Int Commun Heat Mass Transf.* 2016;78:88–94.
13. Hashemian M, Jafarmadar S, Ayed H, Wae-hayee M. Thermal-hydrodynamic and exergetic study of two-phase flow in helically coiled pipe with helical wire insert. *Case Stud Therm Eng.* 2022;30:101718.
14. Wei H, Moria H, Nisar KS, Ghandour R, Issakhov A, Sun YL, et al. Effect of volume fraction and size of Al₂O₃nanoparticles in thermal, frictional and economic performance of circumferential corrugated helical tube. *Case Stud Therm Eng.* 2021;25:100948.
15. Hashemian M, Jafarmadar S, Khalilarya S, Faraji M. Energy harvesting feasibility from photovoltaic/thermal (PV/T) hybrid system with Ag/Cr₂O₃-glycerol nanofluid optical filter. *Renew Energy.* 2022;198:426–39.
16. Hassan MA, Al-Tohamy AH, Kaood A. Hydrothermal characteristics of turbulent flow in a tube with solid and perforated conical rings. *Int Commun Heat Mass Transf.* 2022;134:106000.
17. Hassan MA, Kaood A. Multi-criteria assessment of enhanced radiant ceiling panels using internal longitudinal fins. *Build Environ.* 2022;224:109554.
18. Sinaga N, Khorasani S, Sooppy Nisar K, Kaood A. Second law efficiency analysis of air injection into inner tube of double tube heat exchanger. *Alexandria Eng J.* 2021;60:1465–76.
19. Kaood A, Elhagali IO, Hassan MA. Investigation of high-efficiency compact jet impingement cooling modules for high-power applications. *Int J Therm Sci.* 2023;184:108006.
20. Adio SA, Alo TA, Olagoke RO, Olalere AE, Veeredhi VR, Ewim DRE. Thermohydraulic and entropy characteristics of Al₂O₃-water nanofluid in a ribbed interrupted microchannel heat exchanger. *Heat Transf.* 2021;50:1951–84.
21. Rainieri S, Bozzoli F, Cattani L. Passive techniques for the enhancement of convective heat transfer in single phase duct flow. In: *Journal of physics: conference series.* 2014 (547).
22. Abolarin SM, Everts M, Meyer JP. Heat transfer and pressure drop characteristics of alternating clockwise and counter clockwise twisted tape inserts in the transitional flow regime. *Int J Heat Mass Transf.* 2019;133:203–17.
23. Bhattacharyya S, Pathak M, Sharifpur M, Chamoli S, Ewim DRE. Heat transfer and exergy analysis of solar air heater tube with helical corrugation and perforated circular disc inserts. *J Therm Anal Calorim.* 2021;145:1019–34.
24. Admane AA, Patil PA. Compound heat transfer enhancement in dimpled wall duct fitted with coiled wire insert. *Int J Eng Res.* 2014;3:589–95.
25. Shoji Y, Sato K, Oliver DR. Heat transfer enhancement in round tube using wire coil: influence of length and segmentation. *Heat Transf - Asian Res.* 2003;32:99–107.
26. Naphon P. Effect of coil-wire insert on heat transfer enhancement and pressure drop of the horizontal concentric tubes. *Int Commun Heat Mass Transf.* 2006;33:753–63.
27. Abbaspour M, Mousavi Ajarostaghi SS, Hejazi Rad SAH, Nimaifar M. Heat transfer improvement in a tube by inserting perforated conical ring and wire coil as turbulators. *Heat Transf.* 2021;50:6164–88.
28. Abedin MZ, Sarkar MAR. Experimental study of heat transfer enhancement through a tube with wire-coil inserts at low turbulent reynolds number. *Int J Eng Mater Manuf.* 2018;3:122–33.
29. Vahidifar S, Kahrom M. Experimental study of heat transfer enhancement in a heated tube caused by wire-coil and rings. *J Appl Fluid Mech.* 2015;8:885–92.
30. Ali RK, Sharafeldeen MA, Berbish NS, Moawed MA. Convective heat transfer enhancement inside tubes using inserted helical coils. *Therm Eng.* 2016;63:42–50.
31. Fadodun OG, Amosun AA, Okoli NL, Olaloye DO, Durodola SS, Ogundeji JA. Sensitivity analysis of entropy production in Al₂O₃/H₂O nanofluid through converging pipe. *J Therm Anal Calorim.* 2019;143:431–44.
32. Fadodun OG, Amosun AA, Salau AO, Ogundeji JA. Numerical investigation of thermal performance of single-walled carbon nanotube nanofluid under turbulent flow conditions. *Eng Rep.* 2019;1:e12024.
33. Fadodun OG, Amosun AA, Olaloye DO. Numerical modeling of entropy production in Al₂O₃/H₂O nanofluid flowing through a novel Bessel-like converging pipe. *Int Nano Lett.* 2021;11:159–78.
34. Bahiraei M, Naseri M, Monavari A. Irreversibility features of a shell-and-tube heat exchanger fitted with novel trapezoidal oblique baffles: application of a nanofluid with different particle shapes. *Int Commun Heat Mass Transf.* 2021;126:105352.
35. Mahian O, Kianifar A, ZeinaliHeris S, Wongwises S. First and second laws analysis of a minichannel-based solar collector using boehmite alumina nanofluids: effects of nanoparticle shape and tube materials. *Int J Heat Mass Transf.* 2014;78:1166–76.
36. Benkhedda M, Boufendi T, Tayebi T, Chamkha AJ. Convective heat transfer performance of hybrid nanofluid in a horizontal pipe considering nanoparticles shapes effect. *J Therm Anal Calorim.* 2020;140:411–25.
37. Jeong J, Li C, Kwon Y, Lee J, Kim SH, Yun R. Particle shape effect on the viscosity and thermal conductivity of ZnO nanofluids. *Int J Refrig.* 2013;36:2233–41.

38. Ferrouillat S, Bontemps A, Poncelet O, Soriano O, Gruss JA. Influence of nanoparticle shape factor on convective heat transfer and energetic performance of water-based SiO₂ and ZnO nanofluids. *Appl Therm Eng.* 2013;51:839–51.
39. Maheshwary PB, Handa CC, Nemade KR. A comprehensive study of effect of concentration, particle size and particle shape on thermal conductivity of titania/water based nanofluid. *Appl Therm Eng.* 2017;119:79–88.
40. Yelpale M, Shrivastava R, Nandan G. Heat transfer enhancement and pressure drop in two-phase flow boiling using coiled wire as turbulent promoters: A review. In: *AIP Conference Proceedings 2021* (vol: 2341).
41. Abdelrazek AH, Kazi SN, Alawi OA, Yusoff N, Oon CS, Ali HM. Heat transfer and pressure drop investigation through pipe with different shapes using different types of nanofluids. *J Therm Anal Calorim.* 2020;139:1637–53.
42. Chiam HW, Azmi WH, Adam NM, Ariffin MKAM. Numerical study of nanofluid heat transfer for different tube geometries: a comprehensive review on performance. *Int Commun Heat Mass Transf.* 2017;86:60–70.
43. Launder BE, spalding DB. The numerical computation of turbulent flows. In: *Numerical prediction of flow, heat transfer, turbulence and combustion 1983.* (p. 96–116).
44. Ansys. *Ansys Fluent user's guide.* Ansys fluent user's guid. 2013;15317:2498.
45. Pourfattah F, Akbari OA, Jafrian V, Toghraie D, Pourfattah E. Numerical simulation of turbulent flow and forced heat transfer of water/CuO nanofluid inside a horizontal dimpled fin. *J Therm Anal Calorim.* 2020;139:3711–24.
46. Versteeg HK, Malalasekera W. *An introduction to computational fluid dynamics: the finite volume method.* Pearson education; 2007.
47. Mazaheri N, Bahiraei M. Energy, exergy, and hydrodynamic performance of a spiral heat exchanger: process intensification by a nanofluid containing different particle shapes. *Chem Eng Process - Process Intensif.* 2021;166: 108481.
48. Timofeeva EV, Routbort JL, Singh D. Particle shape effects on thermophysical properties of alumina nanofluids. *J Appl Phys.* 2009;106:014304.
49. Ooi EH, Popov V. Numerical study of influence of nanoparticle shape on the natural convection in Cu-water nanofluid. *Int J Therm Sci.* 2013;65:178–88.
50. T. D. Canonsburg. *Ansys fluent theory guide.* Ansys Inc., USA. Canonsburg, PA, USA, PA, USA; 2013.
51. Dittus FW, Boelter LMK. Heat transfer in automobile radiators of the tubular type. *Int Commun Heat Mass Transf.* 1985;12:3–22.
52. Sieder EN, Tate GE. Heat transfer and pressure drop of liquids in tubes. *Ind Eng Chem.* 1936;28:1429–35.
53. Gnielinski V. New equations for heat and mass transfer in turbulent pipe and channel flow. *Int Chem Eng.* 1976;16:359–68.
54. Petukhov BS. *Heat Transfer and Friction in Turbulent Pipe Flow with Variable Physical Properties.* *Adv Heat Transf.* Elsevier; 1970. p. 503–64.
55. Blasius H. *Das Aehnlichkeitsgesetz bei Reibungsvorgängen in Flüssigkeiten.* Berlin, Heidelberg, Heidelberg: Springer Berlin Heidelberg; 1913. p. 1–41.
56. Filonenko GK. Hydraulic resistance of pipelines. *Therm Eng.* 1954;4:40–4.
57. Ali HM. In tube convection heat transfer enhancement: SiO₂ aqua based nanofluids. *J Mol Liq.* 2020;308:113031.

Publisher's Note Springer Nature remains neutral with regard to jurisdictional claims in published maps and institutional affiliations.